arXiv:1601.01734v1 [quant-ph] 8 Jan 2016

0.54 μm resolution two-photon interference with dispersion cancellation for quantum optical coherence tomography

Masayuki Okano[1,2,3], Hwan Hong Lim[4], Ryo Okamoto[1,2,3], Norihiko Nishizawa[5], Sunao Kurimura[4], and Shigeki Takeuchi[1,2,3,*]

[1]Department of Electronic Science and Engineering, Kyoto University, Kyoto daigaku-katsura, Nishikyo-ku, Kyoto, Kyoto, Japan
[2]Research Institute for Electronic Science, Hokkaido University, Sapporo, Hokkaido, Japan
[3]The Institute of Scientific and Industrial Research, Osaka University, Mihogaoka 8-1, Ibaraki, Osaka, Japan
[4]National Institute for Materials Science, 1-1 Namiki, Tsukuba, Ibaraki, Japan
[5]Department of Quantum Engineering, Nagoya University, Furo-cho, Chikusa-ku, Nagoya, Aichi, Japan
[*]takeuchi@kuee.kyoto-u.ac.jp

ABSTRACT

Quantum information technologies harness the intrinsic nature of quantum theory to beat the limitations of the classical methods for information processing and communication. Recently, the application of quantum features to metrology has attracted much attention. Quantum optical coherence tomography (QOCT), which utilizes two-photon interference between entangled photon pairs, is a promising approach to overcome the problem with optical coherence tomography (OCT): As the resolution of OCT becomes higher, degradation of the resolution due to dispersion within the medium becomes more critical. Here we report on the realization of 0.54 μm resolution two-photon interference, which surpasses the current record resolution 0.75 μm of low-coherence interference for OCT. In addition, the resolution for QOCT showed almost no change against the dispersion of a 1 mm thickness of water inserted in the optical path, whereas the resolution for OCT dramatically degrades. For this experiment, a highly-efficient chirped quasi-phase-matched lithium tantalate device was developed using a novel 'nano-electrode-poling' technique. The results presented here represent a breakthrough for the realization of quantum protocols, including QOCT, quantum clock synchronization, and more. Our work will open up possibilities for medical and biological applications.

Introduction

One of the most distinct feature of quantum physics is quantum entanglement. Entanglement attracted attention first in the test of nonlocality of quantum mechanics,[1–3] and started to be considered as an essential resource for quantum information protocols,[4] including quantum key distribution,[5,6] quantum teleportation,[7,8] and quantum computation.[9–11] Recently, the application of quantum entanglement for metrology and sensing is attracting attention.[12,13] One recent example is an entanglement-enhanced microscope, where a photon-number entangled state is used as probe light to enhance the sensitivity.[14] Here we focus on another example: an application of the frequency entangled state of photons for optical coherence tomography (OCT).[15,16]

OCT based on low-coherence interference (LCI)[17] has been widely used in various fields, including medical applications such as imaging of the retina and cardiovascular system.[15,16] Figure 1a shows a schematic diagram of OCT. Broadband light from a source is divided at a beam splitter (BS). One beam is incident on a sample after passing through a dispersive medium, while the other beam is reflected from a mirror with a temporal delay τ. The OCT interference fringe $I(\tau)$ is obtained by the detection of the interfered light intensity with varying delay τ (Figure 1a inset). When the bandwidth of the source is made broader to achieve higher resolution, the resolution, far from being improved, degrades due to dispersion in the medium. This constitutes a severe problem in OCT.[18] Although dispersion effect can be compensated by inserting a 'phantom', a medium with the same dispersion, in the reference path,[19] it requires *a priori* knowledge of both the structure and the frequency-dependent refractive index of the target object. Furthermore, as the resolution becomes higher, a slight difference between the target object and the 'phantom' becomes a crucial problem.

As an alternative method, quantum optical coherence tomography (QOCT)[20–24] based on the two-photon interference (TPI) of frequency-entangled photon pairs[25] has been proposed[20] (Figure 1b). Broadband entangled photon pairs can be

generated via a spontaneous parametric down-conversion process from a nonlinear crystal. Signal photons reflected at a sample through a dispersive medium and idler photons with a temporal delay τ, interfere quantum mechanically at a BS, and coincidence detection events are counted at two single photon detectors. The QOCT interference dip $C(\tau)$, which is so called Hong-Ou-Mandel (HOM) dip,[25] is obtained by the coincidence count rate with varying delay τ (Figure 1b inset). Due to the frequency correlation of entangled photon pairs, the resolution of QOCT (the width of the HOM dip) does not change even with group velocity dispersion (GVD) in the medium.[26,27] This 'dispersion cancellation' of TPI was first demonstrated with 19 μm resolution[21] and very recently with 3 μm resolution, where the GVD effect becomes significant.[28]

In this work, we report 0.54 μm resolution TPI with dispersion cancellation for ultra-high resolution QOCT. For highly efficient generation of ultra-broadband (166 THz, λ = 660-1040 nm) frequency-entangled photon pairs, we developed a 1st-order chirped quasi-phase-matched (QPM)[29] lithium tantalate[30] device using the nanofabrication technology for fine electrode patterns. The device was pumped using a narrowband ($\sim$ 100 kHz) pump laser to ensure the dispersion cancellation of TPI.[28] We also constructed stable interferometer setup with hybrid ultra-broadband detection systems (HUBDeS) operated at room temperature. In addition, dispersion cancellation in TPI was demonstrated against a 1 mm thickness of water inserted in the optical path. Almost no degradation in resolution was observed for TPI (from 0.54 μm to 0.56 μm), which is in contrast to the significant degradation in LCI resolution (from 1.5 μm to 7.8 μm). The 0.54 μm resolution in air, which corresponds to the resolution of 0.40 μm in water, is the best among the previously achieved LCI resolution 0.75 μm[31] for OCT and also TPI resolutions for QOCT, including that (0.85 μm[23]) where dispersion cancellation was not verified.

Results

The 1st-order QPM device was developed using a 'nano-electrode-poling' technique. Note that the conversion efficiency of the 1st-order QPM[32] is supposed to be almost one order magnitude (9 times) larger than that of the 3rd-order QPM;[22,23] however, it is impossible to realize using conventional photolithography techniques. For high-power ultraviolet pumping, Mg-doped stoichiometric lithium tantalate (Mg:SLT)[30,33] was selected because it has a short absorption edge around 270 nm[34] and high thermal conductivity.[35,36] Furthermore, Mg:SLT is free from visible-light-induced nonlinear infrared absorption, which is observed in Mg:$LiNbO_3$.[37] The new device fabrication process that was employed is shown in Figure 2a. A 500 μm thick Mg:SLT wafer doped with 1.0 mol% Mg was used to suppress photorefractive damage and a 100 nm thick Al film was evaporated onto the wafer surface. A nanoscale resist pattern was defined using electron beam lithography (EBL) and then transferred to an Al pattern by dry etching on the surface of the Mg:SLT wafer. EBL free from the diffraction limit of light provides over 10 times higher accuracy than photolithography, but special care is required to avoid charge-up in the ferroelectric Mg:SLT substrate. The width of the Al electrode was 400 nm and the duty ratio of the period was approximately 10% to the period assuming reasonable sidewise expansion (scanning electron microscopy (SEM) images are shown in Figure 2b). An electric field of 2 kV/mm was then applied in the vacuum chamber to achieve a high electric field contrast by suppression of the surface screening charge for precise control of the domain duty ratio. Domain sidewise motion was successfully controlled over 6,000 domains along the 20 mm device length with a 6.7% chirped poling period varying from 3.12 to 3.34 μm (optical microscopy images are shown in Figure 2c). Although each EBL scanning area is limited to a width of 200 μm ($\ll$ 20 mm device length), the extremely accurate translation stage enables a 20 nm connection error, which results in a low phase slip between scanned areas. The fluctuation in the domain duty ratio (typically 0.65) was less than 10% to the period (Figure 2c), which suggests uniform conversion efficiency along the entire spectral range.

The experimental setup for the TPI is shown in Figure 3a (Details are given in Methods). The chirped QPM Mg:SLT device is set in a temperature controlled metal holder (Figure 3a upper inset). The temperature T is controlled by a thermoelectric cooler with an accuracy of 0.1 K. We have found that in ultra-high resolution regime the linewidth of a pump laser degrades the dispersion tolerance.[28] To ensure the dispersion tolerance, we used a narrowband pump laser ($\sim$ 100 kHz) with a wavelength of 401 nm. The pump beam is focused to a diameter of 80 μm with a lens; this diameter is sufficiently smaller than the cross-section of the device (500 μm (vertical) $\times$ 800 μm (horizontal)), and then cut by filters after the device. Collinearly emitted photons had ultra-broad bandwidth with a device temperature $T = 351$ K as shown in Figure 3b. The spectrum spans from 660 nm with a sharp rise. We think that the offset in the shorter wavelength region ($\leq$ 650 nm) is stray fluorescence from the device. Considering the frequency correlation with the center wavelength of 802 nm, the spectrum should span up to 1040 nm with a bandwidth of 166 THz. The low intensity in the longer wavelength region ($\geq$ 950 nm) may be due to the low coupling efficiency to the optical fiber for the spectrometer we used. Figure 3c shows non-collinearly emitted photon pairs (signal photons and idler photons) with an emission angle of 1.5 degrees relative to the pump beam with a device temperature $T = 353$ K. With the detection event of a signal photon as a trigger, the coincidence count rate of the idler photons was typically 5% (5×10^5 Hz) that of the single photon count rate ($\sim 1\times10^7$ Hz). Signal and idler photons coupled to fiber couplers (FCs) are transferred to the TPI interferometer through polarization-maintaining fibers. The delay τ is determined by the physical position of the FC. The coincidence count rate $C(\tau)$ is obtained by two HUBDeSs, which consist of a Si avalanche photodiode (APD) with a detection bandwidth spanning from 400 to 1060 nm and an InGaAs APD with a bandwidth spanning from 950 to

1150 nm. For the LCI experiments, we used signal photons as a low-coherence light source with the exactly same bandwidth of the source for TPI and the HUBDeS 1 for detection (Figure 3a lower inset). For the check of the dispersion effect, a 1 mm thickness of water enclosed by two thin glass cover plates is inserted in the optical paths of both TPI and LCI interferometers. Note that according to the conventional definition for OCT,[16] the interferograms below are expressed in units of the 'delay' $c\tau/2$, where c is the speed of light, considering the physical displacement of the delay mirrors in OCT and QOCT systems (Figure 1).

The experimental results are shown in Figure 4. First, the LCI signal was obtained as plotted by the red dots in Figure 4a. The full width at half maximum (FWHM) of the interference fringe is 1.5 μm, which is slightly larger than the FWHM of 1.1 μm for theoretical calculation (blue line in Figure 4a) assuming a rectangular spectral shape with a 166 THz bandwidth. We think that this degradation is induced by the GVD: When the thicknesses of the glass of BS in the optical paths of the probe beam and the reference beam (Figure 3a lower inset) are different, the degradation occurs by the GVD of the glass. We have found that the difference of the FWHMs can be explained when we assume that the difference of the thicknesses of the glass is just 150 μm.

Figure 4b shows the LCI signal when a 1 mm thickness of water is inserted in the optical path. Due to the GVD of the 1 mm thickness of water,[38] the interference fringe becomes much broader. The FWHM of the fringe is 7.8 μm, which is more than 5 times larger than that without the 1 mm thickness of water sample. These results illustrate how GVD effect becomes crucial in ultra-high resolution regime.

The main results of this paper are shown in Figures. 4c and 4d. Figure 4c shows the TPI signal without the water sample. The FWHM of the observed HOM dip is 0.54$\pm$0.05 μm, which surpasses 0.75 μm of LCI[31] for OCT using a broadband laser light with a center wavelength of 725 nm, which is the current best record resolution as far as we know. The resolution of 0.54 μm in air corresponds to the resolution of 0.40 μm in water or biological tissue. The theoretical curve (blue line in Figure 4c) assuming the observed spectrum of the signal photons (Figure 3c) fits well with the experimental data. Note that for the same bandwidth of the photon source with a rectangular shaped spectrum, the FWHM of the TPI is a half of the LCI,[28] which is also an advantage of QOCT especially when the bandwidth of the optical window is limited.

Finally, experimental demonstration of the dispersion cancellation of an ultra-high resolution TPI for QOCT is shown in Figure 4d. The HOM dip is almost unchanged from Figure 4c even when a 1 mm thickness of water is inserted in the optical path, which is in striking contrast to the case of LCI (Figures. 4a and 4b). The FWHM of the HOM dip is 0.56$\pm$0.04 μm and the difference between the FWHMs with and without the 1 mm thickness of water is 0.02 μm, which is smaller than the margins of errors. The theoretical curve (blue line in Figure 4d) calculated taking the higher-order dispersion of the 1 mm thickness of water[38] into account fits also well with the experimental data. Note that the asymmetricity of the HOM dip observed in the experimental data is due to the higher odd-order dispersion,[28,39] which can be also observed in the theoretical curve. Our theoretical calculation suggests that the resolution will be still kept 0.60 μm even when a thickness of water is increased to 3 mm. For thicker medium, 'phantom' can also be used to compensate the dispersion effect for QOCT, similar to OCT. In case of QOCT, the thickness of the phantom does not have to be exactly the same with the medium due to the inherit dispersion cancellation by frequency entanglement demonstrated here. In case of OCT, on the other hand, the thickness or the GVD of the phantom has to be exactly the same with the medium as we discussed on Figure 4a, which is technically very difficult. The detail of the theoretical estimation of FWHMs and the calculation are given in Methods.

Conclusion

In conclusion, we have achieved 0.54 μm resolution TPI with dispersion cancellation for ultra-high resolution QOCT, which surpasses the current record resolution 0.75 μm of LCI for OCT. We developed a 1st-order chirped QPM Mg:SLT device using a 'nano-electrode-poling' technique with EBL for ultra-broadband entangled photon pair generation (166 THz, λ = 660-1040 nm). A 6.7% chirped poling period varying from 3.12 to 3.34 μm was fabricated in over 6,000 domains along a 20 mm long device. We constructed stable interferometers with HUBDeSs that consist of commercially available single photon detectors operated at room temperature. In addition, dispersion cancellation was demonstrated in TPI against a 1 mm thickness of water inserted in the optical path. Almost no degradation in resolution was observed in TPI (from 0.54 μm to 0.56 μm), whereas the LCI resolution was significantly degraded (from 1.5 μm to 7.8 μm). These results will open the door to ultra-high resolution QOCT imaging with depth resolution less than half a micrometer. Such ultra-high resolution QOCT will be beneficial for many different areas, for example, following up the change of the retinal thickness with the ultra-high resolution will greatly help the early detection of glaucoma.[40] For this end, the increase in the flux of entangled photons is very important. The flux of 0.3 μW has already been realized using bulk QPM devices.[41–43] Further increase in flux up to tens of μW can be expected using slab or ridge type waveguide structures.[44,45] A promising direction may be an OCT/QOCT hybrid system where OCT is used for a quick wide-range scan and QOCT is used when ultra-high resolution / high precision observation is required. We also note that the ultra-high resolution TPI with dispersion cancellation demonstrated here is useful for quantum protocols, including not only QOCT but also quantum clock synchronization,[46] time-frequency entanglement measurement[47]

and multimode frequency entanglement.[48]

Methods

Details of experimental setup

The pump laser system consists of a single-frequency continuous wave Ti:sapphire laser (MBR-110, Coherent) excited by a diode-pumped solid state laser (Verdi G-10, Coherent) and a resonant frequency doubling unit (MBD-200, Coherent). The output of the Ti:sapphire laser (wavelength: 802 nm; linewidth: approximately 100 kHz) is frequency doubled by second-harmonic generation. It is used as the pump beam with a power of 100 mW. This narrow linewidth ($\sim$ 100 kHz) ensures the dispersion tolerance of TPI in ultra-high resolution regime.[28] We treated the narrowband pump beam as a monochromatic pump for numerical calculations based on the theory.[28,39] The focused pump beam at the chirped quasi-phase-matched device has a confocal parameter (i.e., twice the Rayleigh length) of 18 mm.

For the measurements of frequency spectra, generated entangled photons from the device are coupled to the the polarization-maintaining fiber and sent to a 300-mm spectrometer with a 150-grooves/mm grating blazed at 800 nm (SP-2358, Princeton Instruments) and a charge coupled device (CCD) camera (Pixis:100BRX, Princeton Instruments). The transmission efficiency of the spectrometer and the quantum efficiency of the CCD camera were calibrated in Figures 3b and 3c.

Each of HUBDeS shown in Figure 3a consists of a Si APD (SPCM-AQRH-14, Perkin Elmer) and an InGaAs APD (id401, idQuantique). The coincidence count rate C between two HUBDeSs is obtained by the sum of coincidence counts between two APDs as $C = C_{\text{Si-1/Si-2}} + C_{\text{Si-1/InGaAs-2}} + C_{\text{Si-2/InGaAs-1}} + C_{\text{InGaAs-1/InGaAs-2}}$, where for example $C_{\text{Si-1/InGaAs-2}}$ is the coincidence count rate between Si APD 1 in HUBDeS 1 and InGaAs APD 2 in HUBDeS 2. The coincidence time window of the coincidence counter (id800, idQuantique) was 2 ns.

Analysis of interference signals

For LCI experimental data (plotted by red dots in Figures 4a and 4b), a FWHM of interference fringe is determined by the full width at the middle between a base line and a peak height. The base line is the average of the whole interference fringe along the delay. The peak height is calculated using the smallest or largest data point. In theoretical calculations for LCI (blue lines in Figures 4a and 4b), we calculated based on the theory[28] assuming a rectangular spectral shape with a center wavelength of 802 nm and a bandwidth of 166 THz for the light source. In the case with a 1 mm thickness of water inserted in the optical path, we assumed the 2nd-order dispersion and the 3rd-order dispersion of the water.[38] For TPI experimental data (red dots in Figures 4c and 4d), a FWHM of interference dip is determined by the FWHM of a Gaussian fitting curve (black dashed lines in Figures 4c and 4d). The Gaussian fit uses the whole range of the dip along the delay and assumes the experimental visibility. The experimental visibilities of dips with and without the water dispersion are 0.67 ± 0.05 and 0.73 ± 0.04, respectively. In theoretical calculations for TPI (blue lines in Figures 4c and 4d), we assumed the observed spectrum of the signal photons (Figure 3c), experimental coincidence count rate and experimental visibilities. We also assumed the GVD and the 3rd-order dispersion of the water[38] for the case with the 1 mm thickness of water inserted.

References

1. Einstein, A., Podolsky, B. & Rosen, N. Can quantum-mechanical description of physical reality be considered complete? *Phys. Rev.* **47**, 777–780 (1935).
2. Bell, J. S. On the Einstein-Podolsky-Rosen paradox. *Physics* **1**, 195–200 (1964).
3. Aspect, A., Dalibard, J. & Roger, G. Experimental test of Bell's inequalities using time-varying analyzers. *Phys. Rev. Lett.* **49**, 1804–1807 (1982).
4. Kimble, H. J. The quantum internet. *Nature* **453**, 1023–1030 (2008).
5. Ekert, A. K. Quantum cryptography based on Bell's theorem. *Phys. Rev. Lett.* **67**, 661–663 (1991).
6. Gisin, N. & Thew, R. Quantum communication. *Nat. Photonics* **1**, 165–171 (2007).
7. Bennett, C. H., Brassard, G., Crépeau, C., Jozsa, R., Peres, A. & Wootters, W. K. Teleporting an unknown quantum state via dual classical and Einstein-Podolsky-Rosen channels. *Phys. Rev. Lett.* **70**, 1895–1899 (1993).
8. Bouwmeester, D., Pan, J.-W., Mattle, K., Eibl, M., Experimental quantum teleportation. *Nature* **390**, 575–579 (1997).
9. Knill, E., Laflamme, R. & Milburn, G. J. A scheme for efficient quantum computation with linear optics. *Nature* **409**, 46–52 (2001).
10. Ladd, T. D., Jelezko, F., Laflamme, R., Nakamura, Y., Monroe, C. & O'Brien, J. L. Quantum computers. *Nature* **464**, 45–53 (2010).

11. Okamoto, R., O'Brien, J. L., Hofmann, H. F. & Takeuchi, S. Realization of a Knill-Laflamme-Milburn controlled-NOT photonic quantum circuit combining effective optical nonlinearities.. *Proc. Natl. Acad. Sci.* **108**, 10067–10071 (2010).

12. Giovannetti, V., Lloyd, S. & Maccone, L. Quantum-enhanced measurements: beating the standard quantum limit. *Science* **306**, 1330–1336 (2004).

13. Nagata, T., Okamoto, R., O'Brien, J. L., Sasaki, K. & Takeuchi, S. Beating the standard quantum limit with four-entangled photons. *Science* **316**, 726–729 (2007).

14. Ono, T., Okamoto, R. & Takeuchi, S. An entanglement-enhanced microscope. *Nat. Commun.* **4**, 2426 (2013).

15. Huang, D., Swanson, E. A., Lin. C. P., Schuman, J. S., Stinson, W. G., Chang, W., Hee, M. R., Flotte, T., Gregory, K., Puliafito, C. A., & Fujimoto, J. G. Optical coherence tomography. *Science* **254**, 1178–1181 (1991).

16. Brezinski, M. *Optical Coherence Tomography.* (Academic Press, 2006).

17. Born, M. & Wolf, E. *Principles of Optics.* (Cambridge University Press, 1999).

18. Hitzenberger, C. K., Baumgartner, A., Drexler, W. & Fercher, A. F. Dispersion effects in partial coherence interferometry: implications for intraocular ranging. *J. Biomed. Opt.* **4**, 144–151 (1999).

19. Drexler, W, Morgner, U, Ghanta, R. K, Kärtner, F. X, Schuman, J. S, & Fujimoto, J. G. Ultrahigh-resolution ophthalmic optical coherence tomography. *Nat. Med.* **7**, 502–507 (2001).

20. Abouraddy, A. F., Nasr, M. B., Saleh, B. E. A., Sergienko, A. V., & Teich, M. C. Quantum-optical coherence tomography with dispersion cancellation. *Phys. Rev. A* **65**, 053817 (2002).

21. Nasr, M. B., Saleh, B. E. A., Sergienko, A. V., & Teich, M. C. Demonstration of dispersion-canceled quantum-optical coherence tomography. *Phys. Rev. Lett.* **91**, 083601 (2003).

22. Nasr, M. B, Carrasco, S, Saleh, B. E. A, Sergienko, A. V, Teich, M. C, Torres, J. P, Torner, L, Hum, D. S, & Fejer, M. M. Ultrabroadband biphotons generated via chirped quasi-phase-matched optical parametric down-conversion. *Phys. Rev. Lett.* **100**, 183601 (2008).

23. Nasr, M. B, Minaeva, O, Goltsman, G. N, Sergienko, A. V, Saleh, B. E, & Teich, M. C. Submicron axial resolution in an ultrabroadband two-photon interferometer using superconducting single-photon detectors. *Opt. Express* **16**, 15104–15108 (2008).

24. Nasr, M. B., Goode, D. P., Nguyen, N., Rong, G., Yang, L., Reinhard, B. M., Saleh, B. E. A. & Teich, M. C. Quantum optical coherence tomography of a biological sample. *Opt. Comm.* **282**, 1154–1159 (2009).

25. Hong, C. K, Ou, Z. Y, & Mandel, L. Measurement of subpicosecond time intervals between two photons by interference. *Phys. Rev. Lett.* **59**, 2044–2046 (1987).

26. Steinberg, A. M, Kwiat, P. G, & Chiao, R. Y. Dispersion cancellation in a measurement of the single-photon propagation velocity in glass. *Phys. Rev. Lett.* **68**, 2421–2424 (1992).

27. Steinberg, A. M, Kwiat, P. G, & Chiao, R. Y. Dispersion cancellation and high-resolution time measurements in a fourth-order optical interferometer. *Phys. Rev. A* **45**, 6659–6665 (1992).

28. Okano, M, Okamoto, R, Tanaka, A, Ishida, S, Nishizawa, N, & Takeuchi, S. Dispersion cancellation in high-resolution two-photon interference. *Phys. Rev. A* **88**, 043845 (2013).

29. Harris, S. E. Chirp and compress: Toward single-cycle biphotons. *Phys. Rev. Lett.* **98**, 063602 (2007).

30. Yu, N. E, Kurimura, S, Nomura, Y, & Kitamura, K. Stable high-power green light generation with thermally conductive periodically poled stoichiometric lithium tantalate. *Jpn. J. Appl. Phys.* **43**, L1265 (2004).

31. Povazay, B, Bizheva, K, Unterhuber, A, Hermann, B, Sattmann, H, Fercher, A. F, Drexler, W, Apolonski, A, Wadsworth, W. J, Knight, J. C, Russell, P. S. J, Vetterlein, M, & Scherzer, E. Submicrometer axial resolution optical coherence tomography. *Opt. Lett.* **27**, 1800–1802 (2002).

32. Fejer, M, Magel, G, Jundt, D, & Byer, R. Quasi-phase-matched second harmonic generation: tuning and tolerances. *IEEE J. Quantum Electron.* **28**, 2631–2654 (1992).

33. Lim, H. H., Kurimura, S., Katagai, T. & Shoji, I. Temperature-dependent Sellmeier equation for refractive index of 1.0 mol% Mg-doped stoichiometric lithium tantalate. *Jpn. J. Appl. Phys.* **52**, 032601 (2013).

34. Nalwa, H. S. (Eds.) *Volume 4: Ferroelectrics and Dielectrics, Handbook of Advance Electronic and Photonic Materials and Devices.* (Academic Press, 2001).

35. Tovstonog, S. V, Kurimura, S, Suzuki, I, Takeno, K, Moriwaki, S, Ohmae, N, Mio, N, & Katagai, T. Thermal effects in high-power cw second harmonic generation in mg-doped stoichiometric lithium tantalate. *Opt. Express* **16**, 11294–11299 (2008).

36. Lim, H. H, Katagai, T, Kurimura, S, Shimizu, T, Noguchi, K, Ohmae, N, Mio, N, & Shoji, I. Thermal performance in high power SHG characterized by phase-matched calorimetry. *Opt. Express* **19**, 22588–22593 (2011).

37. Hirohashi, J., Tago, T., Nakamura, O., Miyamoto, A. & Furukawa, Y. Characterization of GRIIRA properties in $LiNbO_3$ and $LiTaO_3$ with different compositions and doping. *Proc. SPIE* **6875**, 687516 (2008).

38. Van Engen, A. G, Diddams, S. A, & Clement, T. S. Dispersion measurements of water with white-light interferometry. *Appl. Opt.* **37**, 5679–5686 (1998).

39. Okamoto, R, Takeuchi, S, & Sasaki, K. Tailoring two-photon interference with phase dispersion. *Phys. Rev. A* **74**, 011801 (2006).

40. Asrani, S., Challa, P., Herndon, L., Lee, P., Stinnett, S. & Allingham, R. R. Correlation among retinal thickness, optic disc, and visual field in glaucoma patients and suspects: A pilot study. *J. Glaucoma* **12**, 119–128 (2003).

41. Dayan, B., Pe'er, A., Friesem, A. A. & Silberberg, Y. Nonlinear interactions with an ultrahigh flux of broadband entangled photons. *Phys. Rev. Lett.* **94**, 043602 (2005).

42. Sensarn, S, Ali-Khan, I, Yin, G. Y, & Harris, S. E. Resonant sum frequency generation with time-energy entangled photons. *Phys. Rev. Lett.* **102**, 053602 (2009).

43. Tanaka, A, Okamoto, R, Lim, H. H, Subashchandran, S, Okano, M, Zhang, L, Kang, L, Chen, J, Wu, P, Hirohata, T, Kurimura, S, & Takeuchi, S. Noncollinear parametric fluorescence by chirped quasi-phase matching for monocycle temporal entanglement. *Opt. Express* **20**, 25228–25238 (2012).

44. Kurimura, S., Kato, Y., Maruyama, M., Usui, Y. & Nakajima, H. Quasi-phase-matched adhered ridge waveguide in LiNbO3. *Appl. Phys. Lett.* **89**, 191123 (2006).

45. Kou, R., Kurimura, S., Kikuchi, K., Terasaki, A., Nakajima, H., Kondou, K. & Ichikawa, J. High-gain, wide-dynamic-range parametric interaction in Mg-doped LiNbO3 quasi-phase-matched adhered ridge waveguide. *Opt. Express* **19**, 11867–11872 (2011).

46. Giovannetti, V, Lloyd, S, Maccone, L, & Wong, F. N. C. Clock synchronization with dispersion cancellation. *Phys. Rev. Lett.* **87**, 117902 (2001).

47. Hofmann, H. F & Ren, C. Direct observation of temporal coherence by weak projective measurements of photon arrival time. *Phys. Rev. A* **87**, 062109 (2013).

48. Mikhailova, Y. M, Volkov, P. A, & Fedorov, M. V. Biphoton wave packets in parametric down-conversion: Spectral and temporal structure and degree of entanglement. *Phys. Rev. A* **78**, 062327 (2008).

Acknowledgements

The authors thank Shoichi Sakakihara (ISIR, Osaka Univ.) for water sample preparation, Toru Hirohata and Masamichi Yamanishi (Hamamatsu Photonics) for lending ultra-broadband photo multiplier tubes for us, Yu Eto and Akira Tanaka (Osaka Univ.) for helpful discussions. This work was supported in part by the Japan Science and Technology Agency CREST project (JST-CREST), the Quantum Cybernetics project of the Japan Society for the Promotion of Science (JSPS), the Funding Program for World-Leading Innovative R&D on Science and Technology Program of JSPS (FIRST), Grant in-Aids from JSPS; the Project for Developing Innovation Systems of the Ministry of Education, Culture, Sports, Science, and Technology (MEXT), the Network Joint Research Center for Advanced Materials and Devices, the Research Foundation for Opto-Science and Technology, and the Global COE programme.

Author contributions statement

Experiments, measurements and data analysis were performed by M.O. with assistance of R.O. and S.T. Device fabrication was carried out by H.H.L. and S.K. All authors discussed the results and commented on the manuscript at all stages. M.O., S.K. and S.T. wrote the manuscript. The project was supervised by N.N., S.K. and S.T.

Additional information

Competing financial interests

The authors declare no competing financial interests.

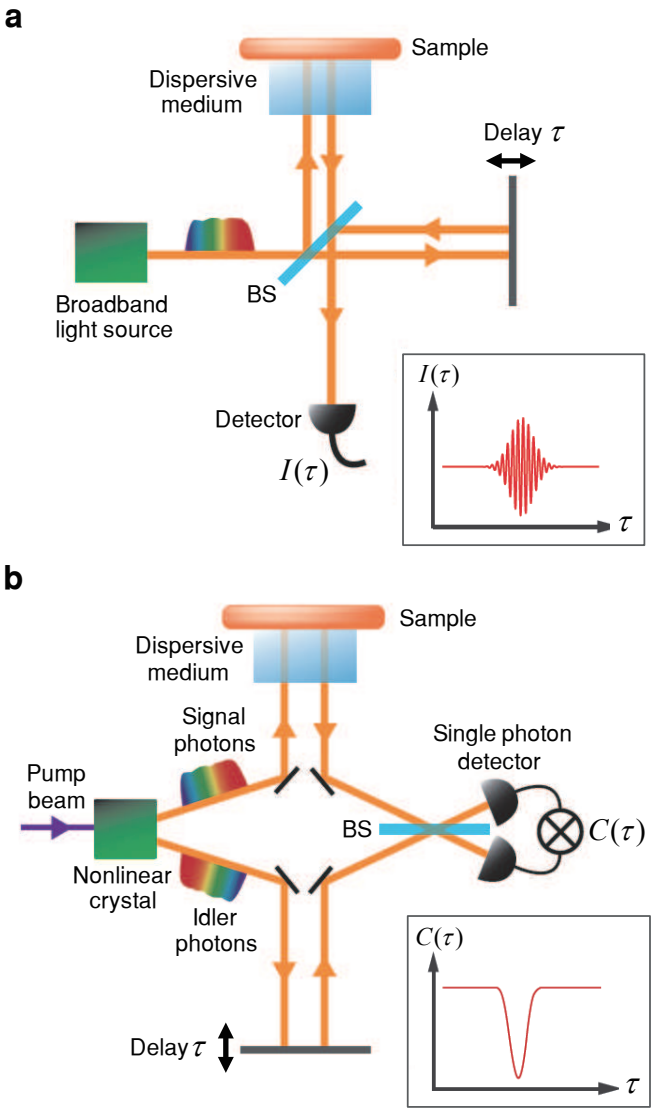


Figure 1. OCT and QOCT schemes. (a), Schematic diagram of OCT. $I(\tau)$ is the interfered light intensity measured at a detector with varying delay τ (inset). BS is a beam splitter. (b), Schematic diagram of QOCT. $C(\tau)$ is the coincidence count rate counted at two single photon detectors with varying delay τ (inset).

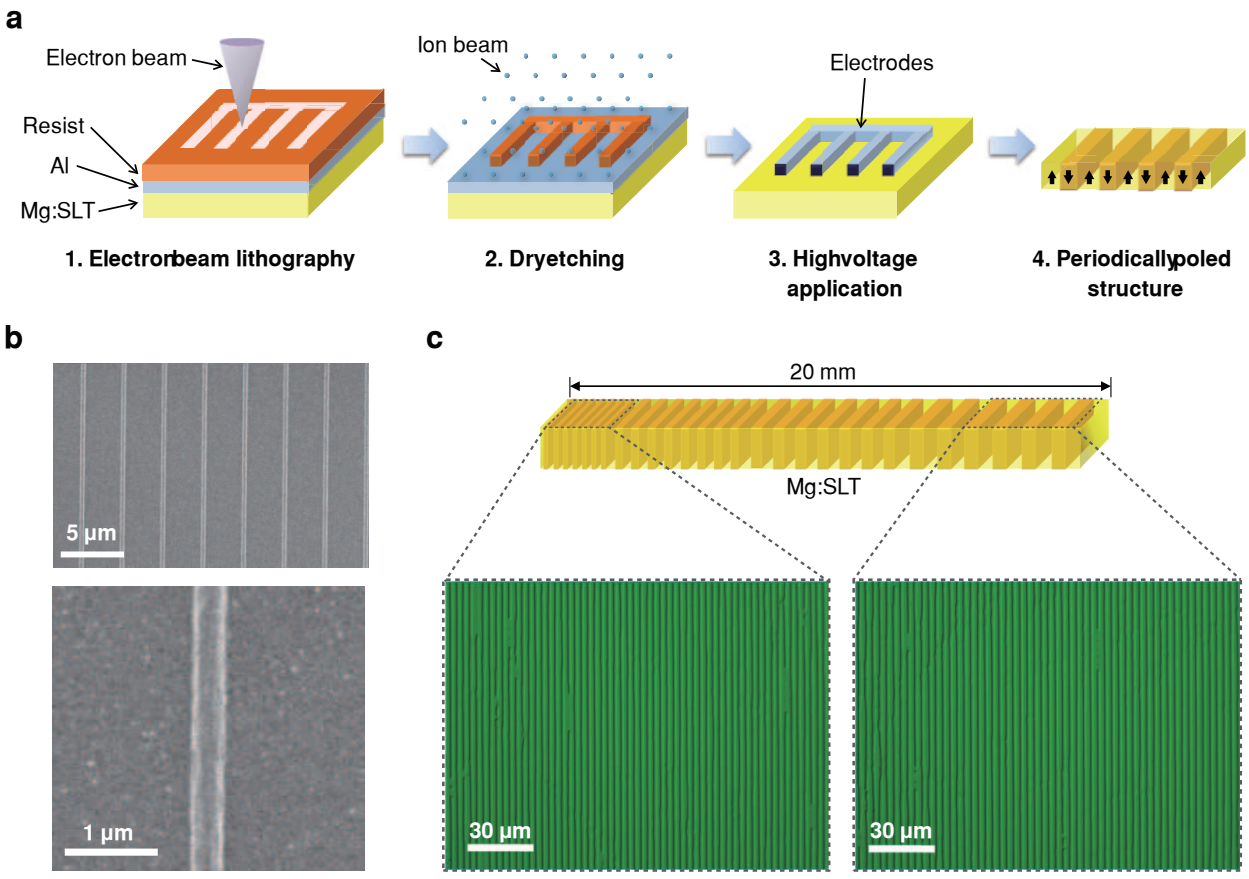


Figure 2. Fabrication of chirped QPM lithium tantalate device using nano-electrode-poling technique. (a), Device fabrication process. Black arrows indicate the direction of ferroelectric spontaneous polarization in the periodically poled device. Mg:SLT is Mg-doped stoichiometric lithium tantalate. (b), Scanning electron microscopy images (upper and lower) of the 400 nm wide Al electrodes fabricated for the poling period of 3.2 μm. (c), Optical Microscopy images of periodically poled structures. The QPM period varies from 3.12 μm (left) to 3.34 μm (right) along the 20 mm device length.

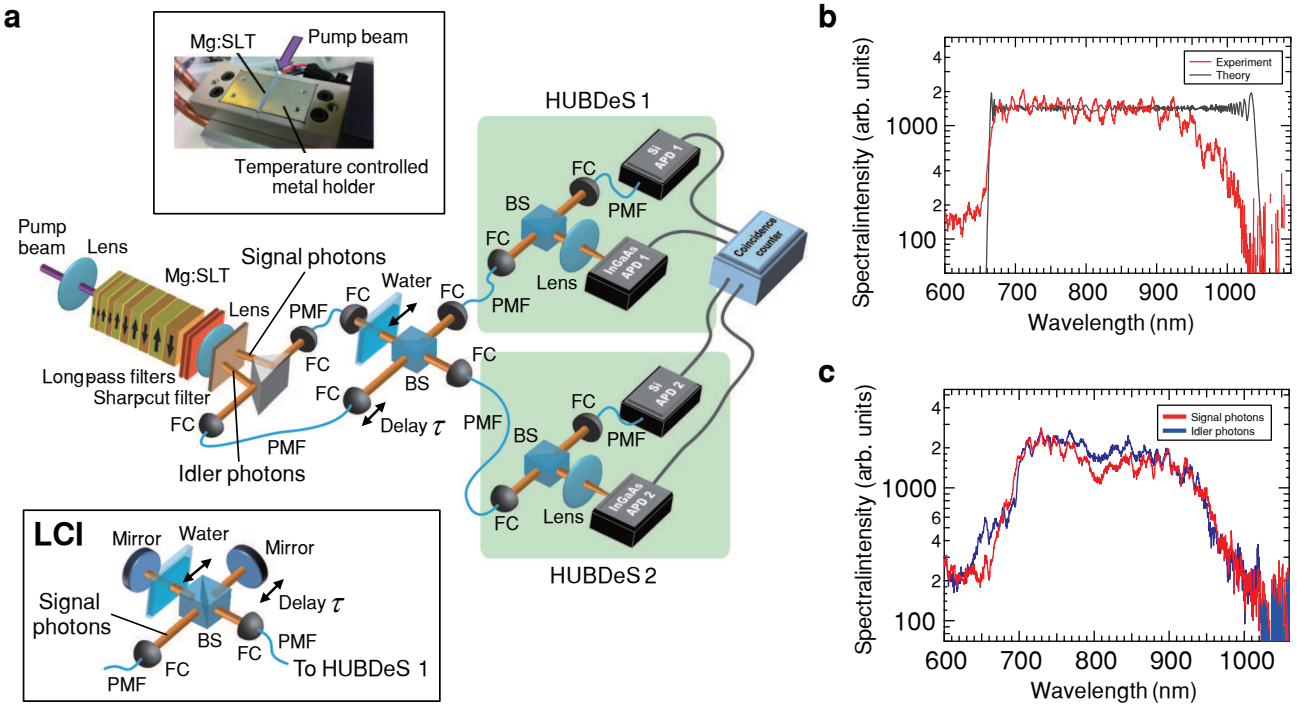


Figure 3. Experimental setup. (a), TPI and LCI interferometers with hybrid ultra-broadband detection systems (HUBDeS). The upper inset shows the chirped QPM device set in the temperature controlled metal holder. HUBDeS consists of a Si avalanche photodiode (APD) and an InGaAs APD. The lower inset shows the LCI interferometer. A 1 mm thickness of water can be inserted in the optical path in TPI and LCI interferometers. BS, beam splitter; FC, fiber coupler; PMF, polarization-maintaining fiber; Mg:SLT, Mg-doped stoichiometric lithium tantalate. (b), Frequency spectrum of collinearly emitted photons from the device. Experimental data (red dots) and the theoretical curve (black line) are plotted. (c), Frequency spectra of photon pairs generated from the device in non-collinear emission. The observed data are plotted for signal photons (red dots) and idler photons (blue dots). The transmission efficiency and detection efficiency of the spectrometer were calibrated (b,c.

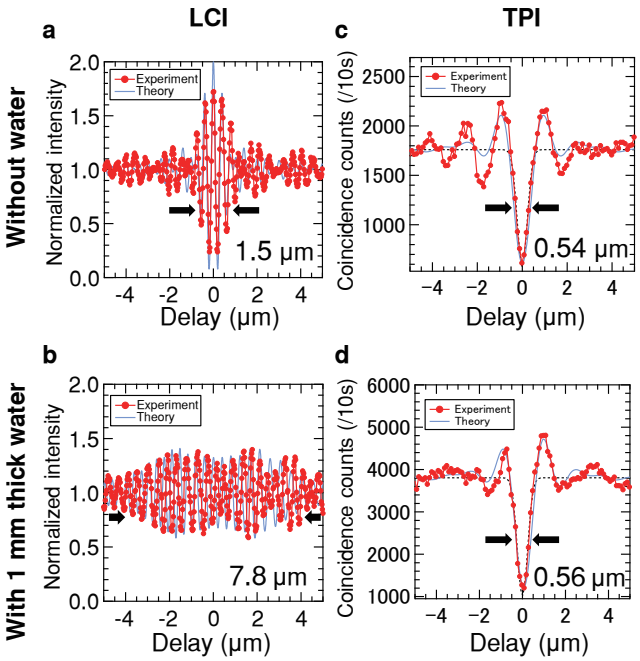


Figure 4. Obtained LCI and TPI signals. (a,b), LCI fringes obtained in the LCI interferometer using signal photons as the source. The fringes without (a) and with (b) a 1 mm thickness of water inserted in the optical path. The experimental data (red dots) and the theoretical curves (blue line) are plotted in units of the delay. The integration time was 1 second per point. (c,d), TPI dips obtained in the TPI interferometer. The dips without (c) and with (d) the 1 mm thickness of water. The experimental data (red dots), the theoretical curves (blue lines) and the Gaussian fitting curves (black dashed lines) are plotted in units of the delay. The integration time was 10 seconds per point. The red lines connecting the data points are a guide to the eye (a–d).